Article (refereed) – Published version

Duchez, Aurelie; Frajka-Williams, Eleanor; Castro, Natalia; Hirschi, Joel; Coward, Andrew. 2014 Seasonal to interannual variability in density around the Canary Islands and their influence on the Atlantic meridional overturning circulation at 26°N. *Journal of Geophysical Research: Oceans*, 119 (3). 1843-1860. 10.1002/2013JC009416

Duchez, Aurelie; Frajka-Williams, Eleanor; Castro, Natalia; Hirschi, Joel; Coward, Andrew. 2014 Seasonal to interannual variability in density around the Canary Islands and their influence on the Atlantic meridional overturning circulation at 26°N. *Journal of Geophysical Research: Oceans*, 119 (3). 1843-1860. 10.1002/2013JC009416

AGU PUBLICATIONS

JGR

Journal of Geophysical Research: Oceans

RESEARCH ARTICLE

10.1002/2013JC009416

Key Points:
- Robust relationship between: density, local WSC, and AMOC
- Density fluctuations drive the UMO transport at seasonal/interannual time scales

Correspondence to:
A. Duchez,
A.Duchez@noc.ac.uk

Citation:
Duchez, A., E. Frajka-Williams, N. Castro, J. Hirschi, and A. Coward (2014), Seasonal to interannual variability in density around the Canary Islands and their influence on the Atlantic meridional overturning circulation at 26°N, *J. Geophys. Res. Oceans*, *119*, 1843–1860, doi:10.1002/2013JC009416.

Received 9 SEP 2013
Accepted 8 FEB 2014
Accepted article online 15 FEB 2014
Published online 13 MAR 2014

Seasonal to interannual variability in density around the Canary Islands and their influence on the Atlantic meridional overturning circulation at 26°N

Aurélie Duchez[1], Eleanor Frajka-Williams[1], Natalia Castro[1], Joël Hirschi[1], and Andrew Coward[1]

[1]Department of Marine Physics and Ocean Climate, National Oceanography Centre, Southampton, UK

Abstract The meridional interior flow obtained from the RAPID array is determined by horizontal density fluctuations at the eastern and western boundary of 26°N. The physical causes of these density variations are responsible for fluctuations in the Atlantic Meridional Overturning Circulation (AMOC) and through it, the meridional heat transport of the Atlantic. In this modeling study, a high-resolution ocean model is used to investigate the source and origin of the AMOC variability associated with the density fluctuations at the eastern boundary. The AMOC in the model is in good agreement with the RAPID observations and appears to adequately represent the smaller scale features of variability around the Canary Islands. In this paper, we identify a robust relationship between the density structure south of the Canary Islands, the local wind stress curl (WSC) around these islands and the AMOC using an empirical orthogonal functions analysis, wavelet transform, and wavelet coherence. We find that the deep density fluctuations at the eastern boundary of 26°N arise from the pumping effect of the spatial pattern of WSC south of the islands. These deep density fluctuations drive the AMOC both on seasonal and interannual time scales, through their influence on the basinwide tilt of the thermocline. At seasonal time scales, the density fluctuations south of the islands are driven by the WSC and directly influence the AMOC. At interannual time scales, a significant coherence is found between the density fluctuation and the southward Upper Mid-Ocean (UMO) transport although the origin of these density fluctuations is not explained by the direct pumping caused by the WSC.

1. Introduction

The ocean and atmosphere redistribute heat around the Earth. At 26°N, the Atlantic Meridional Overturning Circulation (AMOC) accounts for most of the total northward ocean heat transport in the Atlantic ($\sim$1.33 $\pm$ 0.40 PW) [*Johns et al*., 2011], more than 30% of the total heat transport from the tropics to the poles [*Ganachaud and Wunsch*, 2000; *Hall and Bryden*, 1982; *Trenberth and Solomon*, 1994]. Changes in the AMOC and associated heat transport could have severe consequences for Europe's climate [*Vellinga and Wood*, 2002].

The AMOC transport varies on all time scales. In the short term, while modeling studies have shown reasonable representation of the AMOC, the variability tends to be underestimated either on seasonal or interannual time scales [*Matei et al*., 2012; *McCarthy et al*., 2012; *Roberts et al*., 2013]. Long-term climate change projections of the AMOC strength show a wide range of possible behaviors, perhaps due to imperfect representation of AMOC driving mechanisms [*Bigg et al*., 2003; *Stouffer et al*., 2005; *Zickefeld et al*., 2007] and a lack of data records to quantify long-term variability [*Kanzow et al*., 2010]. On millennial time scales, *Ganopolski and Rahmstorf* [2001] suggested that the variability could be associated with unstable ice sheets in the past. On multidecadal time scales, the AMOC heat transport variability is linked with the North Atlantic Oscillation (NAO), which is responsible for the atmospheric heat flux variability [*Delworth and Greatbatch*, 2000; *Eden and Willebrand*, 2001]. On interannual and shorter time scales, the AMOC variations are caused by both fluctuations in the density field and in the wind stress [*Hirschi and Marotzke*, 2007; *Chidichimo et al*., 2010; *Kanzow et al*., 2010]. On very short (subdaily) time scales, the AMOC may undergo large oscillations due to near-inertial gravity waves [*Blaker et al*., 2012]. In order to identify fluctuations on decadal or longer time scales, we must first understand the short term variability of the AMOC.

The RAPID-WATCH/MOCHA array (hereafter referred to as the RAPID array) has been monitoring the AMOC at 26°N since 2004, where the AMOC is computed as the sum of the Florida Straits transport (FST),

Ekman (EKM) transport across 26°N, and the mid-ocean transport above the thermocline (called Upper Mid-Ocean: UMO transport), between the Bahamas and African coast [*Rayner et al*. 2011; *McCarthy et al*. 2012, and references therein]. Since the advent of the RAPID array, the subannual variability of the AMOC has been a topic of interest. Buoyancy forcing is expected to drive density variations on seasonal time scales [*Köhl*, 2005], while eddies and Rossby waves may add a stochastic variability to the AMOC [*Getzlaff et al*., 2005; *Kanzow et al*., 2007; *Hirschi et al*., 2013]. Wind stress variability affects the AMOC through the transbasin Ekman transport as well as upwelling effects at the boundaries. *Köhl* [2005] show that Ekman upwelling at the coasts was responsible for more than 70% of the variability due to winds. *Chidichimo et al*. [2010], however, find that seasonal density fluctuations were coherent down to 1400 m at the eastern boundary, well below the typical Ekman upwelling depths. Instead, wind stress curl (WSC) at the eastern boundary was implicated in the generation of a robust seasonal cycle of the AMOC at 26°N [*Chidichimo et al*., 2010; *Kanzow et al*., 2010]. In particular, *Kanzow et al*. [2010] showed that while both the eastern and western boundary density anomalies contribute to the seasonal cycle of the AMOC, only the eastern boundary seasonal cycle was consistent in amplitude and phase. The observed density fluctuations were in quadrature with localized surface wind forcing (i.e., the WSC led the density anomalies by roughly 90° or 3 months: Figure 16 in their paper), which is expected for upwelling [*Köhl*, 2005; *Kanzow et al*., 2010]. More recently, *Mielke et al*. [2013] show that a high-resolution numerical model adequately captured the seasonal cycle of the AMOC at 26°N, when compared with RAPID observations, but that at 41°N, the modeled and observed seasonal cycles were out-of-phase.

The current study builds on the work of *Chidichimo et al*. [2010] by investigating the relationship between the AMOC and density fluctuations at the eastern boundary of 26°N. Here we use an eddy-resolving numerical ocean model simulating the 1978–2010 period to study the eastern boundary dynamics seen in the RAPID observations in a broader spatial and temporal context. The model is a 1/12° simulation performed with the Nucleus for European Modeling of the Ocean (NEMO) model which is described in section 3. Section 2 describes the physical processes at the eastern boundary of 26°N, section 4 describes the link between the density structure at the eastern boundary, the WSC, and the AMOC. Finally, section 5 summarizes the main results of this paper.

2. Ocean Circulation in the Region of the Canary Islands

The Canary Islands archipelago consists of seven islands, separated by small channels in the North Atlantic just off the African continent. The NW African coast is broadly known as an upwelling region with permanent southward winds. The particulars of upwelling are determined by topography, wind stress variability, and stratification [*Nykjaer and Camp*, 1994; *Knoll et al*., 2002; *Marcello et al*., 2011]. The Canary Islands act as a partial barrier to the Canary Current, an eastern boundary current flowing southward as part of the subtropical gyre, and are a major source of mesoscale activity [*Barton et al*., 1998; *Sangrà et al*., 2009]. The Canary Current continues through the Lanzarote passage, which has been a source of local transport studies for some time now [*Sangrà et al*., 2009; *Fraile-Nuez et al*., 2010; *Marcello et al*., 2011]. These islands generate small-scale variability in the winds and their curl around the islands [*Chavanne et al*., 2002]. This region is also characterized by the presence of a tongue of fresh water south of the Canary Islands, called the Cape Juby upwelling filament (*Barton et al*. [1998] and section 4.1). The generation of the upwelling filament is not well understood, but observations suggest that it is related to the winds [*Barton et al*., 1998], depends on the topography [*Barton et al*., 2004], and directly interacts with the island-generated mesoscale eddies [*Marcello et al*., 2011].

Previously, coastal upwelling and the circulation around the Canary Islands have been the subject of many studies [e.g., *Mittelstaedt et al*., 1991; *Hernández-Guerra et al*., 1993; *Arístegui et al*., 1994; *Barton et al*., 1998; *Knoll et al*., 2002; *Barton et al*., 2004; *Machín et al*., 2006; *Sangrà et al*., 2009; *Fraile-Nuez et al*., 2010 or *Marcello et al*., 2011]. Here, we are concerned with the density fluctuations which may impact the transbasin AMOC rather than with the local circulation, though the two are not independent. In this paper, our area of interest is represented on the bottom left hand corner of Figure 1a and is centered around the Canary Islands. Particular attention will be paid to the coastal area south east of the islands where the four main eastern boundary RAPID moorings are located: EBH2 (27.6°N, 14.2°W, 1400–2000 m), EBH3 (27.8°N, 13.7°W, 1000–4000 m), and EBH4/5 (27.84°N, 13.55°W, 0–1000). The location of these moorings is represented by

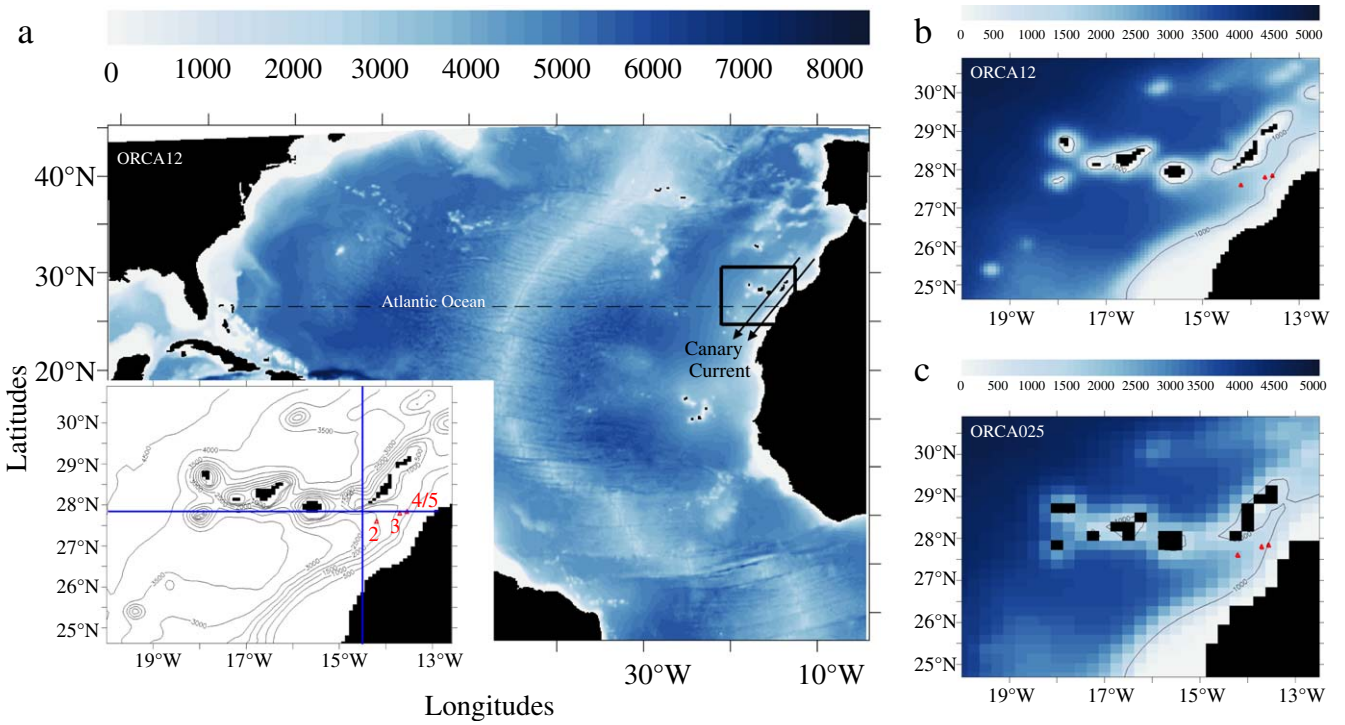

Figure 1. Bathymetry of ORCA12 and ORCA025 in the subtropical North Atlantic. (a) The Canary current is schematically represented by two black arrows. The picture on the left hand corner of Figure 1a represents a zoom on the area of interest centered around the Canary Islands. The three red triangles represent the location of the four eastmost moorings of the RAPID array: EBH2, EBH3, and EBH4/5 (the two different locations of these moorings are not distinguishable at this scale). The locations and depth range of these moorings are given in section 2 [*Rayner et al.*, 2011]. Figures 1b and 1c compare the bathymetry around the Canary Islands in (b) ORCA12 and (c) ORCA025. The mooring positions are also represented on these figures.

red triangles on each panel of Figure 1. This area is strongly influenced by the coastal upwelling and the Cape Juby upwelling filament.

3. Data and Methods

3.1. Model Output

The global ocean-sea ice model simulation used in this study was performed with the NEMO code (Madec and the NEMO Team 2008) in the global ORCA12 configuration set up in the DRAKKAR project (http://www.drakkar-ocean.eu) [*Barnier et al.*, 2006; *DRAKKAR-Group*, 2007]. The horizontal resolution of the configuration grid is 1/12° (4322 × 3059 grid points). At 26°N, the resolution is approximately 8 km, becoming finer at higher latitudes. At this resolution, the configuration is eddy resolving at 26°N. The ORCA12 configuration used to run the simulation was developed from the NEMO 3.2 version and uses the ORCA tri-polar grid (one pole is located in Canada, the other one in Russia, and the last one at the South pole, *Madec and Imbard* [1996]). This configuration has 75 vertical levels with a grid spacing increasing from 1 m near the surface to 200 m at 5500 m. Bottom topography is represented as partial steps and derived from ETOPO2 (National Geophysical Data Center, National Oceanic and Atmospheric Administration, U.S. Dept. of Commerce, 2006, http://www.ngdc.noaa.gov/mgg/global/etopo2.html).

The simulation used in this study was run at the National Oceanography Centre in Southampton (NOCS) with the NEMO-OPA9 code for the ocean dynamics component and output is stored as 5 day averages. This simulation is referred to as ORCA0083-N001 in the DRAKKAR data set but will simply be referred to as ORCA12 in this paper. It was initialized with Levitus [*Atlas et al.*, 2011] in 1978. Here we use the output from 1980 to 2010 (the two first years being removed to reduce the effects of the initialization stage). The DFS4.1 (1978–2005) and DFS5 (2006–2010) surface forcing functions (interannual atmospheric forcings) are used and have been developed by the DRAKKAR consortium. They have a horizontal resolution of 1.125°. As detailed in *Brodeau et al.* [2010], DFS combines elements from two sources: the CORE forcing data set [*Large and Yeager*, 2004], from which precipitation, downward shortwave, and longwave radiation are extracted and the ERA40 reanalysis (for the period 1958–2001) followed by the ECMWF reanalysis (from 2002 to 2010)

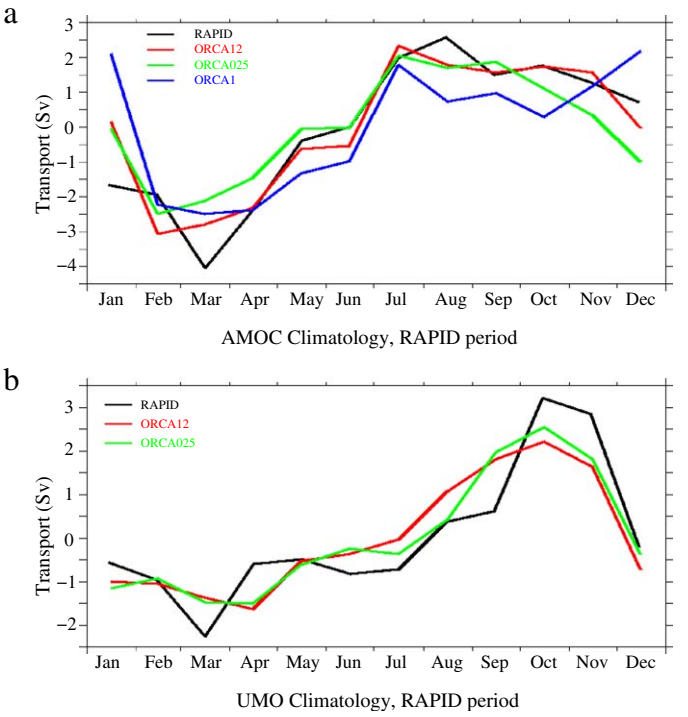

Figure 2. (a) Comparison between the seasonal cycle of the AMOC in RAPID (in black), in ORCA12 (in red), ORCA025 (in green), and ORCA1 (in blue). (b) Comparison between the seasonal cycle of the UMO transport in RAPID (in black), in ORCA12 (in red), and ORCA025 (in green). Monthly mean anomalies are represented in these three figures over the period April 2004 to December 2010 for ORCA12 and the RAPID observations (April 2004 to December 2007 for ORCA1).

which provides 10 m wind, 2 m air humidity, and 2 m air temperature. To compute turbulent air/sea and air/sea-ice fluxes during model integration, the bulk formulae proposed by *Large and Yeager* [2004] are used. The frequency of DFS is monthly for precipitation, daily for radiation, and 6 h for turbulent variables.

The two lower resolution simulations used in this paper (Figure 2) are also extracted from the model NEMO, use an interannual atmospheric forcing, and were run at the NOCS. The 1/4° simulation was run using the ORCA025 configuration and is referred to as ORCA025-VN206ERA in the DRAKKAR data set (it will be referred to as ORCA025 in this paper). This simulation covers the period January 1989 to March 2011 and output is stored as 5 day means. The surface forcing for this simulation is supplied by the ERA Interim forcing [*Dee et al.*, 2011] with a horizontal resolution of the atmosphere of 2.5°. The lowest 1° resolution simulation is called ORCA1 in this paper and is referred to as ORCA1-N403 is the DRAKKAR data set. It covers the period January 1948 to December 2007 and output is stored as monthly means. It is forced by the atmospheric forcing CORE [*Large and Yeager*, 2004] with the same horizontal resolution of 2.5° and monthly mean values are available. To compare the seasonal cycle of the AMOC and UMO transport (Figure 2) in these three NEMO simulations, the period April 2004 to December 2010 is used for ORCA12, ORCA025, and the RAPID observations. Model output from April 2004 to December 2007 is used for ORCA1 (Figure 2a). The seasonal cycle was calculating using monthly means, with the exception of the seasonal cycle of density anomalies displayed in Figure 3, which is using 5 day increments.

3.2. Model Validation

We hypothesize that to represent the fine-scale circulation around the Canary Islands, a high-resolution eddy resolving numerical simulation is needed. The islands of the Canary archipelago as well as the bathymetry near the African coast are better reproduced in the ORCA12 bathymetry than at coarser resolutions. Figure 1 compares the representation of the bathymetry around the Canary Islands in ORCA12 (a and b) and ORCA025 (c). The Canary Islands are absent from the bathymetry of the ORCA1 configuration (not shown in this paper).

Using three NEMO simulations with different horizontal resolutions: 1/12°, 1/4°, and 1° (Figure 2a), we find that the seasonal cycle of the AMOC is in good agreement between RAPID and NEMO. We notice that the seasonal cycle in the ORCA12 simulation is in better agreement with the observations than the two lower resolution simulations. In the three NEMO simulations as well as RAPID, the seasonal cycle of the AMOC is characterized by a minimum around February–March and a plateau from July to the end of the year. During this second part of the year, the AMOC is maximum in August in the observations and 1 month before in the NEMO runs. Although a local maximum is also found in the 1° simulation in July, we notice that its seasonal cycle peaks in December. Details on the influence of the model horizontal resolution on the AMOC variability will be addressed further in the discussion. The main difference between the seasonal cycle of

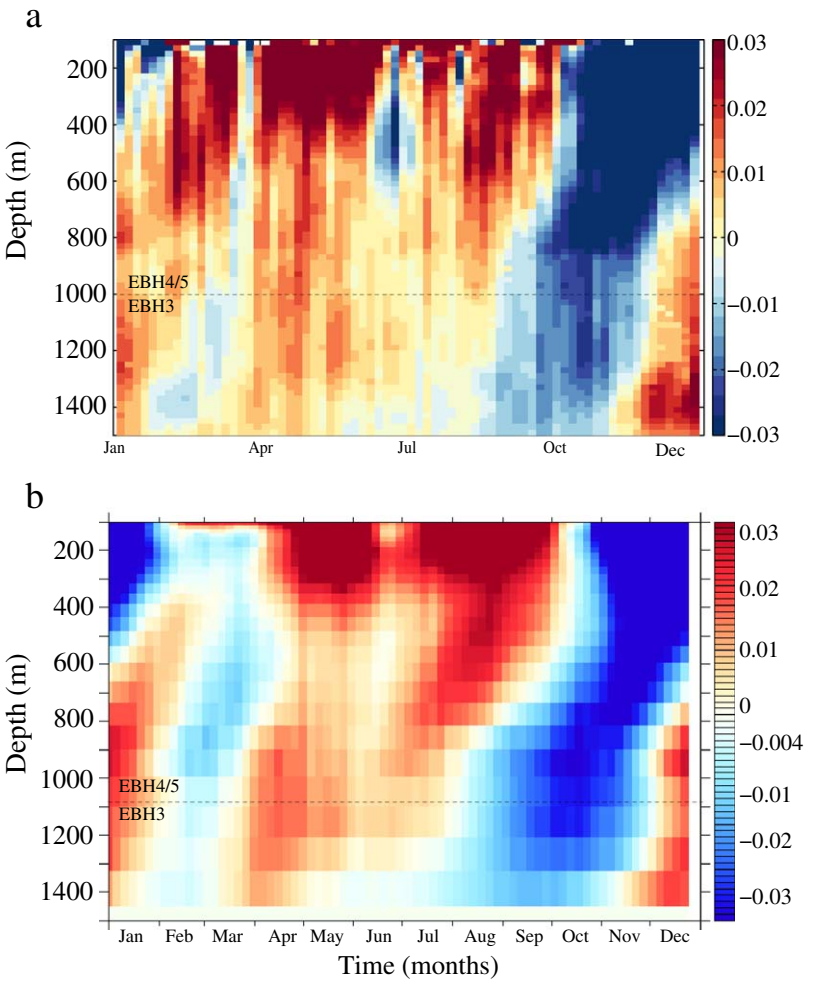

Figure 3. Seasonal cycle of in situ density anomalies (in kg m^{-3}) for (a) RAPID observations and (b) the equivalent for ORCA12. The period 2004–2011 is used for RAPID observations while data from 1980 to 2010 are used for ORCA12. In both cases, the climatologies are computed using 5 day means. For both panels, the density profile is made of densities from the moorings EBH4/5 (27.8°N, 13.55°W) for the top 1000 m, deeper densities (down to 1400 m) come from the mooring EBH3 (27.8°N, 13.75°W).

the AMOC in RAPID and NEMO is the amplitude of the minimum in February–March, which is underestimated (by about 1–2 Sv) in the NEMO simulations. Although the AMOC transport in the RAPID observations is minimum in March, this minimum is reached in February in the three model simulations, which corresponds to a same minimum in the Ekman transport in February in the model output and March in the RAPID observations. This difference in the Ekman transport is partly due to the use of different wind products in RAPID (ERA interim product: *Dee et al*. [2011]) and in the NEMO simulations (DFS4-5).

Figure 2b compares the seasonal cycle of the UMO transport in the RAPID observations and in the 1/12° and 1/4° NEMO simulations. The UMO transport was not calculated for the 1° simulation, since Figure 2a did not show any particular improvement between the seasonal cycle of the AMOC in the 1/4° and 1° simulations. The UMO transport is the southward meridional transport flowing above the thermocline east of the Bahamas and west of the Canaries and is defined as the geostrophic flow in the upper 1000 m. It is primarily governed by the density variations at the western and eastern boundaries of the basin. In particular, variations in the density at the eastern boundary around the Canary Islands are directly associated with fluctuations in the UMO transport, and through it, the AMOC [*Kanzow et al*., 2010]. Using the model simulation, the UMO transport is inferred from zonal density gradients and the thermal wind relation [*Hirschi et al*., 2003]. The full density section, rather than boundary densities, is used in the calculation, but *Hirschi and Marotzke* [2007] have shown that this makes no difference to the calculated geostrophic flow. Depth-averaged velocity is removed to get vertical shear. The result is then integrated zonally and vertically. More

details about the calculation of this transport using RAPID observations are provided in section 3.3. Since the total UMO is southward, a positive UMO anomaly corresponds to a weakening of this transport while a negative anomaly corresponds to an increased UMO transport. For both the observations and the NEMO output, the seasonal cycle of the UMO transport has the weakest southward transport around October and the strongest around March or April [*Kanzow et al*., 2010] although the amplitudes of these extrema are underestimated in the model output. As for the AMOC transport, we notice that the maximum in the UMO transport is reached in March in the RAPID observations but in April in the model simulations.

In order to understand the vertical structure of the seasonal cycle of deep densities, in situ density anomalies in the water column are extracted at single mooring locations and the seasonal cycles are presented in Figure 3. In the RAPID calculation, the density profile in the east is composed of densities from the moorings EBH4/5 for the top 1000 m; deeper densities (down to 1400 m) are from EBH3 (see Figure 1 for mooring positions). As the shallowest instruments of the RAPID moorings are deeper than 100 m, we compare density anomalies between 100 m and 1400 m. The longest available period (1980–2010) is used for the density profile from ORCA12 (Figure 3b), while the period 2004–2011 is used to compute the density profile in the RAPID observations (Figure 3a). Although the comparison is done at a single mooring location (or single grid point for ORCA12), the pattern of density in ORCA12 (Figure 3b) is similar as the RAPID observations: stronger density anomalies are found above 600 m with two maxima, one around April–May, the second one around August–September, and a minimum around November–December. Deeper densities anomalies are also similar in the two data sets with positive anomalies around 1000 m during the first half of the year followed by negative anomalies from August to December. Moreover, as found by *Chidichimo et al*. [2010] using RAPID observations through 2007, ORCA12 shows a seasonal cycle in density anomalies with some anomalies coherent down to 1400 m at the mooring locations.

The general agreement between the RAPID observations and the model results provides the basis for further studying the origins of density fluctuations at the eastern boundary and their imprint on the UMO transport and the AMOC.

3.3. Transport Calculation at 26°N

In this section, we review the link between the density around the Canary Islands and the transbasin transport calculations from the RAPID array. Full details of the transport calculations can be found in *Rayner et al*. [2011]. The component of the AMOC associated with the basinwide transport (between the Bahamas and the Canary Islands) is called the UMO transport and is calculated as the sum of three components:

$$UMO = \int_{-h_{MAX}}^{0} [T_{INT}(z) + T_C(z) + T_{WBW}(z)]dz, \tag{1}$$

where T_{INT} is the interior geostrophic transport per unit depth, T_C a compensation term which insures zero residual transport across 26°N, and T_{WBW} (for Western Boundary Wedge), a transport determined from current meter measurements near the Bahamas. The limit of integration, h_{MAX}, represents the depth of maximum overturning of the AMOC.

Here we are concerned with the geostrophic interior transport, the depth-integrated T_{INT}, determined as:

$$INT = \int_{-h_{MAX}}^{0} T_{INT}(z)dz = -\frac{g}{\rho^* f}\int_{-h_{MAX}}^{0}\left[\int_{-h_{BOT}}^{z}[\rho_E(z') - \rho_W(z')]dz'\right]dz, \tag{2}$$

where h_{BOT} represents the depth of the ocean at this eastern boundary location, g is the acceleration due to gravity, f the Coriolis parameter, ρ^* a reference density, and ρ_E and ρ_W, the densities at the eastern and western boundary of the array, respectively.

Equation (2) shows that the transbasin interior transport (*INT*) depends on the densities at the eastern boundary between h_{MAX} (here fixed at 1000 m) and the bottom. The top 1000 m transport is the integral of density between the bottom (h_{BOT}) and the region above it (with the upper limit of the integral ranging from the surface to 1000 m). In this way, the densities below 1000 m affect the basinwide tilt of the isopycnal layers above. To explain the link between the density at the eastern boundary, the UMO and the AMOC,

we will thus focus on the densities from 1000 m to the bottom. Although we are interested in the link between the density field at the eastern boundary (directly linked to the interior transport) and the AMOC at 26°N, the UMO transport encompassing the three components described in equation (1) will be further used for comparisons with the density field and the WSC around the Canary Islands.

4. Results

The aim of this section is to describe the hydrographic characteristics and temporal variability of the density field at the eastern boundary of 26°N and relate them to the WSC fluctuations around the Canary Islands. The source of these density fluctuations and their influence on the AMOC variability on seasonal to interannual time scales will also be assessed.

4.1. Physical Structure at the Eastern Boundary of 26°N in ORCA12

Surface waters are generally fresh and cold along the African coast, indicative of persistent upwelling at these latitudes. The maximum upwelling occurs in July in this area as the equatorward winds peak at this time of the year [*Barton et al*., 1998]. During this coastal upwelling season, the WSC tends to be cyclonic near the coastal boundary and anticyclonic in the offshore portions [*Bakun and Nelson*, 1991]. With a lag of 3 months (as shown later in the result section of this paper, Figure 10), this maximum anticyclonic offshore WSC drives a minimum in October in the southward UMO transport (Figure 2b). Figures 4a and 4c show the averaged sea surface temperature (a) and salinity (c) for the month of October 1988. An individual snapshot highlights the higher variability in the spatial structure of the temperature and salinity. For this particular month (Figures 4a and 4c) as well as for the 31 year averages (Figures 4b and 4d), coastal upwelling appears along the coast.

This persistent upwelling along the northwest African coast modifies the density structure south of the islands and contributes to the formation of an upwelling filament (Figures 4a and 4c). The Cape Juby upwelling filament (a cold tongue of water south of the Canary Islands) also appears in the model around 27.5°N in the long-term averages. This filament intensifies in the autumn, the period of increased transport in the subtropical gyre and coastal upwelling (not shown here). ORCA12 represents the fine-scale structures known to be present around the Canary Islands (see section 2). Both mesoscale eddies as well as the filament are present in the model output, south of the islands. Mesoscale eddies are visible in the monthly averaged SST (Figure 4a) as well as in the averaged velocities in the top 100 m for October 1988 (Figure 4e). The upwelling filament extends westward and is twisted into a cyclonic eddy located from 16.5°W to 14.5°W and 26.5°N to 27.5°N. Waters from the upwelling filament contain a mix of waters from the subtropical gyre (waters carried by the Canary Current), coming from the north of the islands, and waters from the upwelling region in the Northwest African coast [*Barton et al*., 2004].

Sections through the filament (at 14.5°W) show its vertical structure and intensity (Figure 5). The zonal velocities of the filament are strong (40 cm s^{-1}) westward currents between 27.5 and 28°N, extending down to approximately 1000 m (Figure 5a). Isopycnals are deflected downward just south of the Canary Islands, indicating lighter water in this region than the area around it. This meridional density gradient may affect zonal transport through the thermal wind relation (Figure 5b). The model shows the presence of a permanent cyclonic eddy at 26.5–28°N (called C7 in *Barton et al*. [2004]), with westward flow on the north side merging with the westward flow of the filament.

4.2. Spatial Patterns of Density Fluctuations at 27.8°N

To determine the spatial structure of the dominant mode of variability around the Canaries in the 31 years of model output, we apply empirical orthogonal function (EOF) analysis to the density field at 27.84°N, the latitude of the RAPID moorings EBH4/5 (this section is represented by a horizontal blue line in Figure 1a). Details of the EOF methodology can be found in *Preisendorfer* [1988]. Anomalies (with respect to the long-term mean) of potential densities are used to compute these EOFs. A linear trend was also removed to reduce signals linked to model drift. Since we are interested in seasonal and longer time scales, the model output is first smoothed with a 100 day running mean before calculating the EOFs.

The first two EOFs explain approximately 67% of the variance in this zonal section. The first mode accounts for 44.6% of the variance (Figure 6a). If we focus on the region between 15.5°W and the African coast, this first mode has a vertical structure characterized by three main layers: the Ekman layer (from the surface to

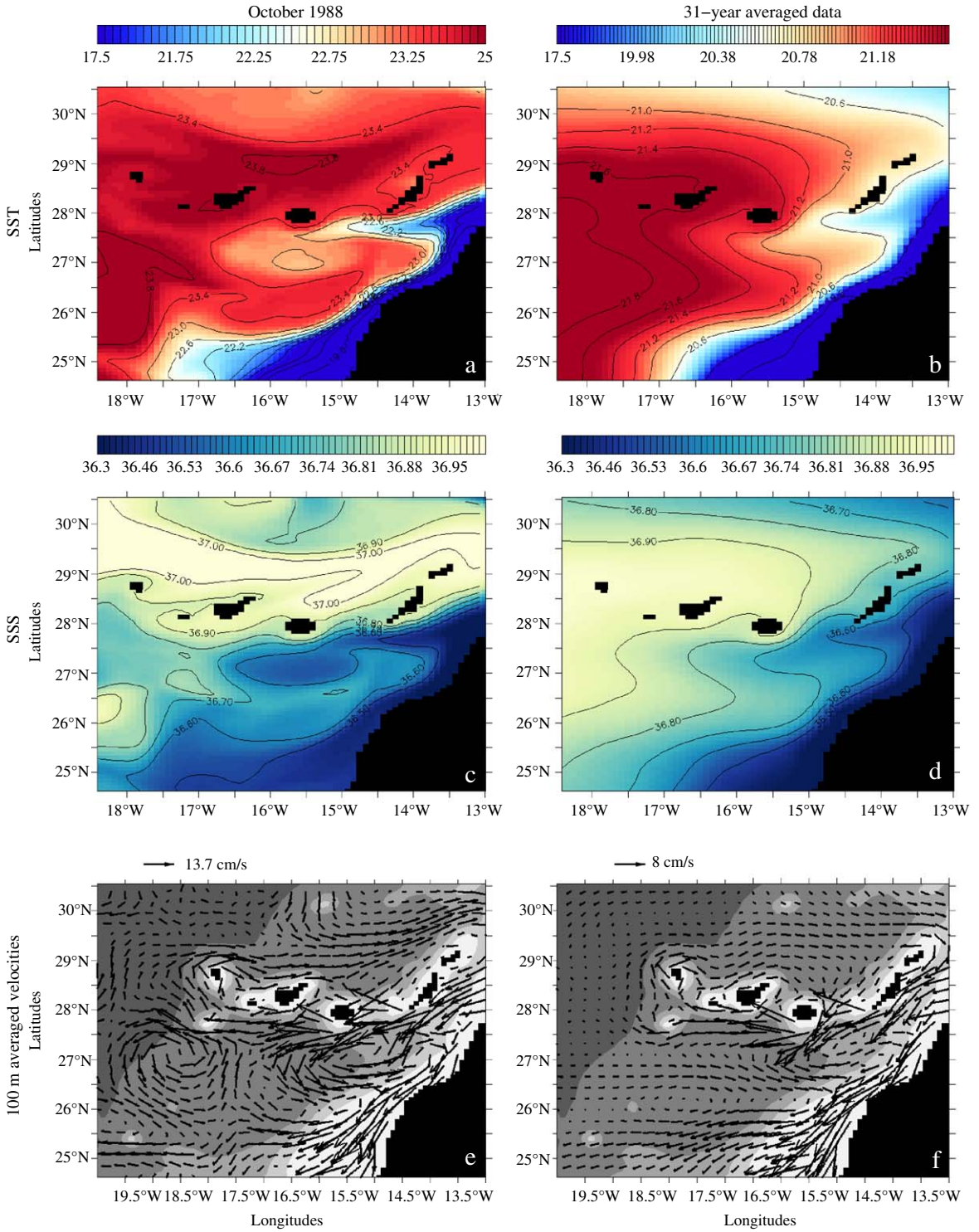

Figure 4. (a and b) SST (in °C), (c and d) SSS, and (e and f) velocities (in m s^{-1}) averaged over the top 100 m in ORCA12. Figures 4a, 4c, and 4e show an average over the month of October 1988 while Figures 4b, 4d, and 4f represent 31 year averaged data (from 1980 to 2010). The grey background on the velocity pictures represents the bathymetry of ORCA12 with changes in the colorscale every 1000 m. The colorbars of the SSS figures are the same for the snapshot and the 31 year averaged data. Two different colorbars are used for the SST figures.

approximately 200 m), another layer between 200 m and 700 m, and the last one from 700 m to the bottom. The first and third layers have the same sign of variability. This spatial EOF pattern also exhibits the coastal upwelling around 13.5°W as denser waters from around 1000 m upwell along the continental slope

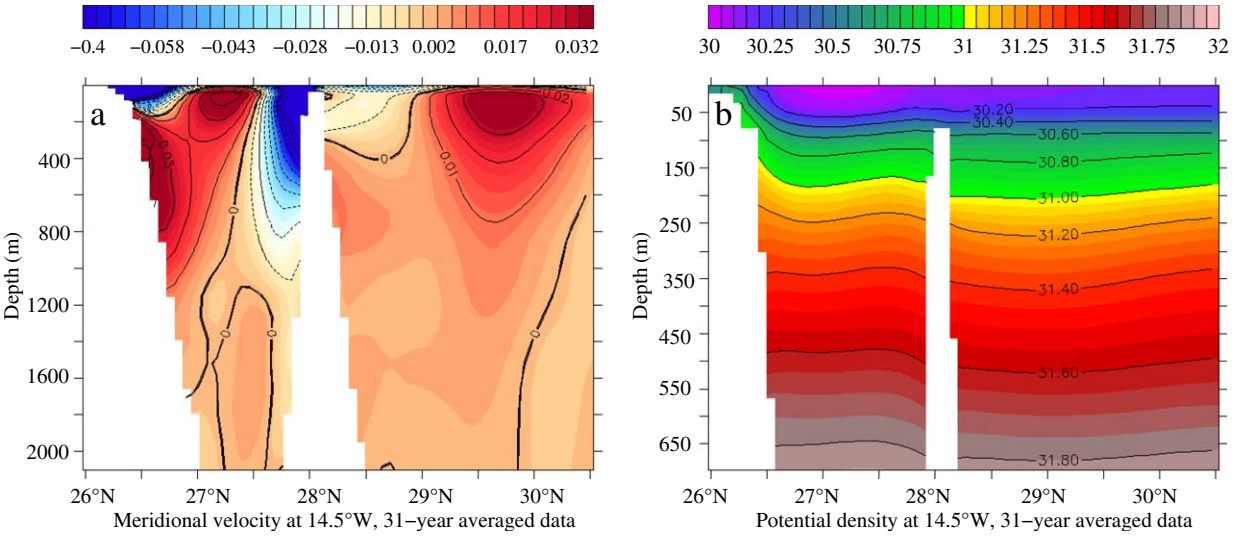

Figure 5. (a) Meridional section (14.5°W) of 31 year averaged zonal velocities (in m s^{-1}) from the 1/12° model output. The location of this section is represented in Figure 1 by a blue vertical line. (b) Same meridional section of 31 year averaged potential density at 14.5°W (in m^3 s^{-1}). The Canary Islands appear on this section as a vertical protrusion of land around 28°N. A zoom on the first 700 m is shown in Figure 5b to highlight the presence of an eddy in the top first 100 m.

up to the surface mainly during the summer. The second mode, accounting for 22% of the variance, shows opposite signs above and below 1500 m (Figure 6b) in reasonable agreement with the density structure identified by *Chidichimo et al*. [2010] (Figure 3 compared to Figure 5 in their paper).

The principal components associated with the first two EOFs are shown in Figure 6e. The seasonal cycle dominates the variability of the first principal component, with a weak interannual signal, while the second mode shows more low-frequency variability with maxima at the beginning and end, and a minimum around 1997–1998. This indicates that the variability in the density structure in this area is dominated by seasonal fluctuations although some interannual fluctuations are found in the two first EOF. The wavelet analysis (Figure 9c) confirms that most of the energy in the first mode of variability of density is found at seasonal time scales. Some energy is also found for periods around 8 years although they are not significant at the 95% level.

The percentage of variance given for each mode in the legends of Figures 6a and 6b accounts for the variability of the full section. To highlight the "center of action" of each mode, homogeneous correlation maps have been computed (Figures 6c and 6d). These maps are obtained from the correlation between the principal component and the time series of the original density data at each grid cell. Areas covered with black cross show correlations significant at the 95% level (Figures 6c and 6d). The extrema associated with mode 1 are located in the top hundred meters of the Ekman layer as well as below 700 m (with 95% significant correlations around 1500 m) and show that the deeper density anomalies have the strongest signal. Mode 2 is focused on the layer from the bottom of the Ekman layer down to 1500 m. As mode 2 does not show any significant correlation with the original density data in our area of interest and explains a small fraction of the total variability, mode 1 will be used to explain the variability in potential density.

4.3. Spatial Patterns of the Wind Stress Curl Around the Canary Islands

To explore the link between the density anomalies and the WSC as suggested by the RAPID data [*Chidichimo et al*., 2010; *Kanzow et al*., 2010], we compute EOFs of the spatial maps of WSC (Figure 7) using the model output for the same time period (1980–2010) and smoothing the time series by a 100 day filter.

The first mode of variability displays a structure with patches of alternating sign, mainly south of the islands, between 19°W and 15°W (Figure 7a), the middle patch including the Canary Islands. This pattern of variability is characteristic of eastern boundary current regions [*Bakun and Nelson*, 1991]. The second mode of variability also displays a similar spatial structure with patches of alternating sign mainly north of the islands with opposite signs compared with the first EOF. These two first modes account for 32.4% and 21.6% of the variance, respectively. The homogeneous correlation maps (Figures 7c and 7d) show that the patterns of

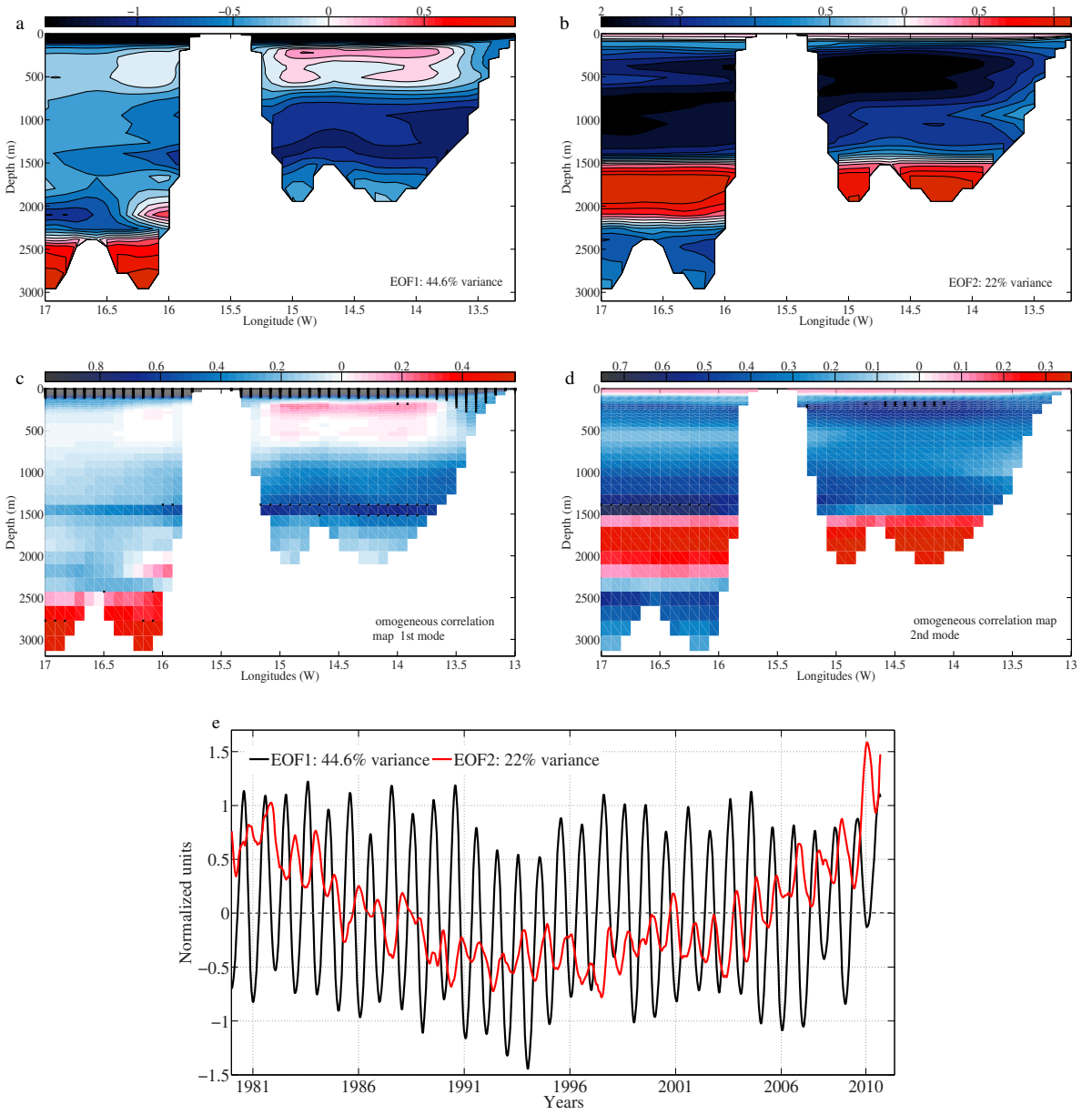

Figure 6. Empirical orthogonal functions (EOFs) analysis for the zonal and vertical structure in potential density anomaly at 27.84°N in the 1/12° model output. This latitude corresponds to the latitude of the RAPID moorings EBH4/5 and is represented by a blue horizontal line in Figure 1. Figures 6a and 6b represent the spatial pattern of the two first modes of variability. Figures 6c and 6d represent homogeneous correlation maps, that is, the correlation between the time series of the EOF mode and the time series of the original density data at each point. Stippled in black are the areas where the correlations are 95% significant. Figure 6e represents the principal components associated with the two first EOFs.

variability south of the islands in the first mode of WSC are 95% significant. Figure 7d shows that a pattern of variability south of Tenerife (between 26.5 and 28°N) is also 95% significant, which means that the second mode of variability does not only describe the variability north of the islands. In the following, we will however still consider that the second mode of variability mainly describes the WSC variability north of the islands.

This different variability north and south of the islands as well as the spatial patterns characterized by three patches of alternating sign on each side of the islands confirm the result shown by *Jiménez et al*. [2008] using annual WSC data, that the presence of the islands influences the wind patterns over this area and hence, impact the spatial variability of the WSC.

The principal components of the first two EOFs of the WSC (Figure 7e) are dominated by the seasonal cycle. These two modes also display interannual variability with a significant change in amplitude from 2001 and

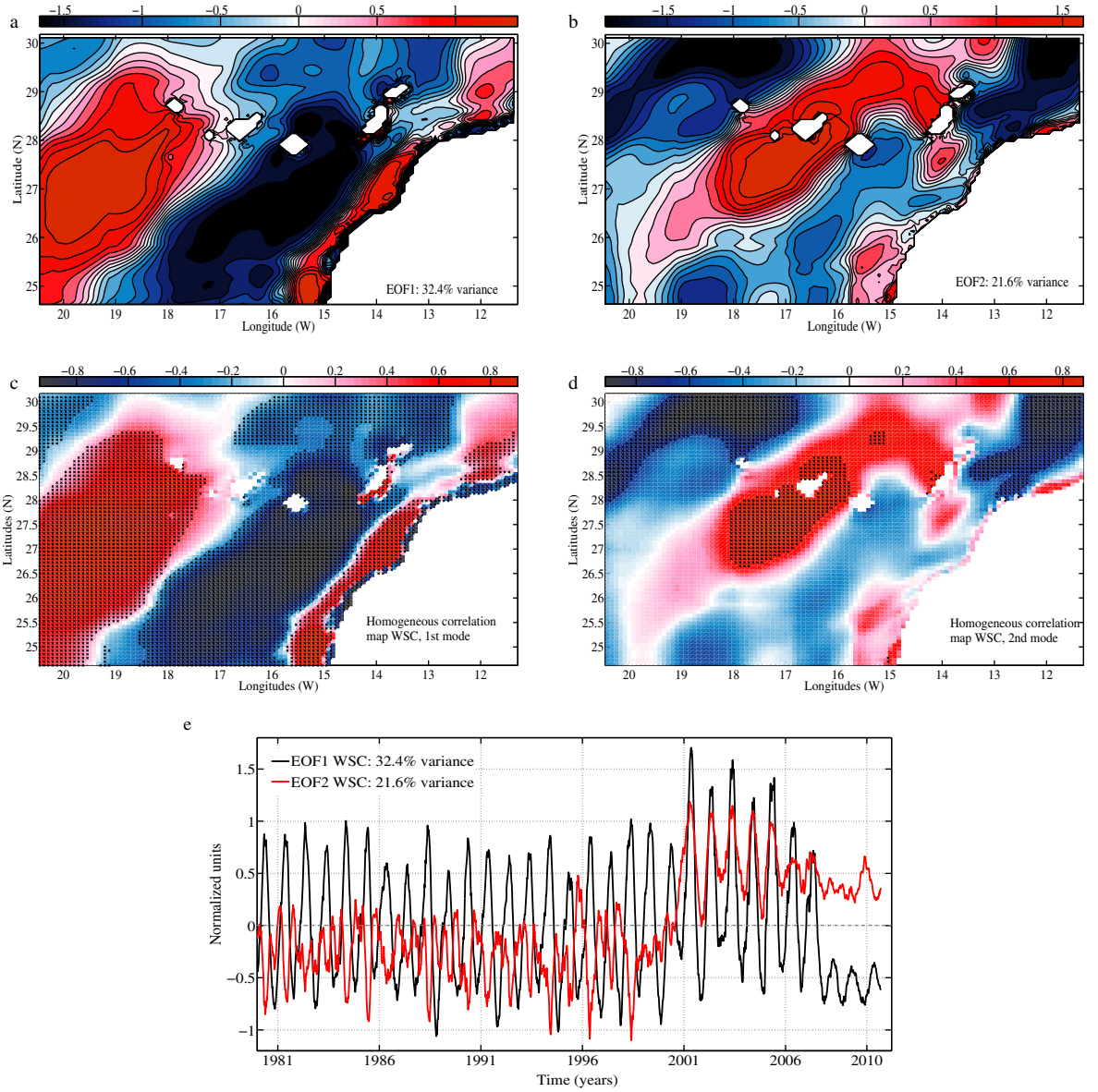

Figure 7. Empirical orthogonal functions (EOFs) analysis for the wind stress curl around the Canary Islands in the 1/12° model output. Figures 7a and 7b represent the spatial variability of the first two modes. Figures 7c and 7d represent the associated homogeneous correlation maps. Stippled in black are the areas where the correlations are 95% significant. Figure 7e shows the principal components associated with the two first EOFs. Hundred day smoothed data are represented in Figure 7e.

another one from 2006, although the anomaly in 2001 is more pronounced in the second mode. As explained in the section describing the simulation used in this study, the anomaly in 2001 is due to a change in the wind forcing (from ERA40 to ECMWF). The anomaly in 2006 is due to a change in the atmospheric forcing (from DFS4.1 to DFS5). The wavelet analysis (Figures 9a and 9b) confirms that most of the energy in the first two modes of variability in WSC is found at seasonal time scales. While the first mode has the strongest seasonal cycle and no significant energy at interannual time scales, the second mode of variability shows energy at period of 4 years and longer, mostly associated with the change in the wind forcing previously described. The EOF analysis and wavelets of the principal component time series were also calculated for the period 1980–2001 only. The wavelet results (not shown) were not visibly altered over the 1980–2001 period (Figure 10). To be able to analyze the longest time series available, and not only assess the seasonal but also interannual variability in the density and WSC fields, model output is still analyzed up to 2010. The wavelet coherence analysis allows us to clearly identify the impact of the change in the atmospheric forcing in 2001 while working with data throughout 2010 (Figures 9 and 10).

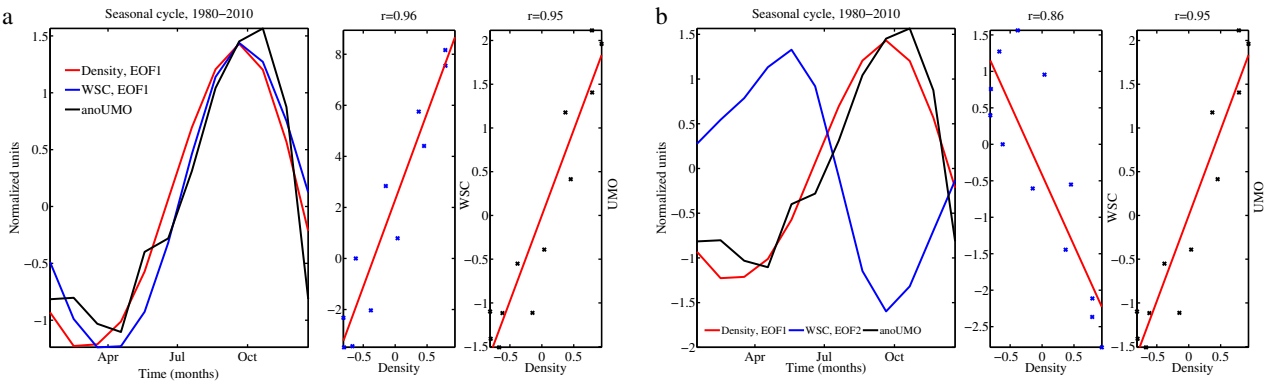

Figure 8. Comparison between the seasonal cycle of the principal components of potential density at 27.84°N (red), time-integrated wind stress curl (blue), and UMO transport at 26°N (black) for the period 1980–2010. Figure 8a compares the first modes of density and wind stress curl while Figure 8b compares the first mode of density and second mode of wind stress curl. To the right of the time series, the scatter plot and linear regression are shown between density and wind stress curl (second plot) and density and UMO transport (third plot). The third figure comparing the wind stress curl and UMO are identical in both panels.

4.4. Relating the Wind Stress Curl to Density Fluctuations

To be able to assess the link between the WSC and the density at 27.8°N at seasonal and interannual time scales, their principal components have been compared. For the seasonal variability, their principal components are directly compared (Figure 8) and the WSC time series has been integrated in time to represent the expected effect of the curl on the local density field (the WSC is only time-integrated in Figure 8). At interannual time scales, wavelet coherence is used to investigate the link between the density and the WSC not only in the frequency but also time domain. Only coherence at a 95% level of significance will be described in this section.

4.4.1. At Seasonal Time Scales

Amplitudes of the first modes for density and time-integrated WSC are significantly correlated with a correlation of 0.96 from 1980 to 2010 (Figure 8a) and 0.95 if data from 1980 to 2001 are used (not shown here). Hence, the time series of density and WSC are 90° out of phase with the WSC preceding the density meaning that the WSC anomalies lead density anomalies south of the islands (this is expected as the WSC is time-integrated in Figure 8). The wavelet coherence analysis confirms these results with large common power between the first EOF of WSC and density (Figure 10a) at seasonal time scales. The arrows in Figure 10 indicate the lag at which they occur. If an arrow is pointing to the right, the two time series are in phase, if it is pointing to the left, they are considered as anti-phase. The deflection of the arrows indicates the lag (e.g., a 90° clockwise deflection for a period of 1 year means that the first time series is leading the second one by 3 months). In Figure 10a and at seasonal time scales (period around 1 year), the arrows pointing downward show the 3 month lag between these two time series.

At seasonal time scales, the second mode of variability of time-integrated WSC is significantly correlated with the first mode of variability of density with a correlation of 0.91 only if data from 1980 to 2001 are used (not shown here). Indeed, the strong anomaly in the WSC in 2001 leads to an anticorrelation between these two time series if data from 1980 to 2010 are considered (Figure 8b). The coherence analysis shows that the WSC and the density have similar power at seasonal time scales for the period 1985–2000 with the density leading the WSC fluctuations by 4 months (Figure 10b). For the period 2001–2007, significant coherence is also found between these data sets with the WSC leading the density anomalies by 3 months. This change in the relationship between these two EOFs is not considered to be significant as it is only due to the change in the wind product used to force the simulation.

A link between the WSC, the vertical velocities at 100 m, and the vortex stretching term dw/dz (where w is the vertical velocity) was investigated by *Sinha et al.* [2013] down to 650 m. The results here are in good agreement with *Sinha et al.* [2013], showing the same limit around 700 m (Figures 6a and 10e). In addition, we show here that the WSC influences the density structure down to the bottom at 2000 m.

4.4.2. At Interannual Time Scales

Given the range of time scales present in the principal components, we use wavelet coherence to identify the links between the WSC and the density. For the period from 1980 to 2010, wavelet coherence analyses

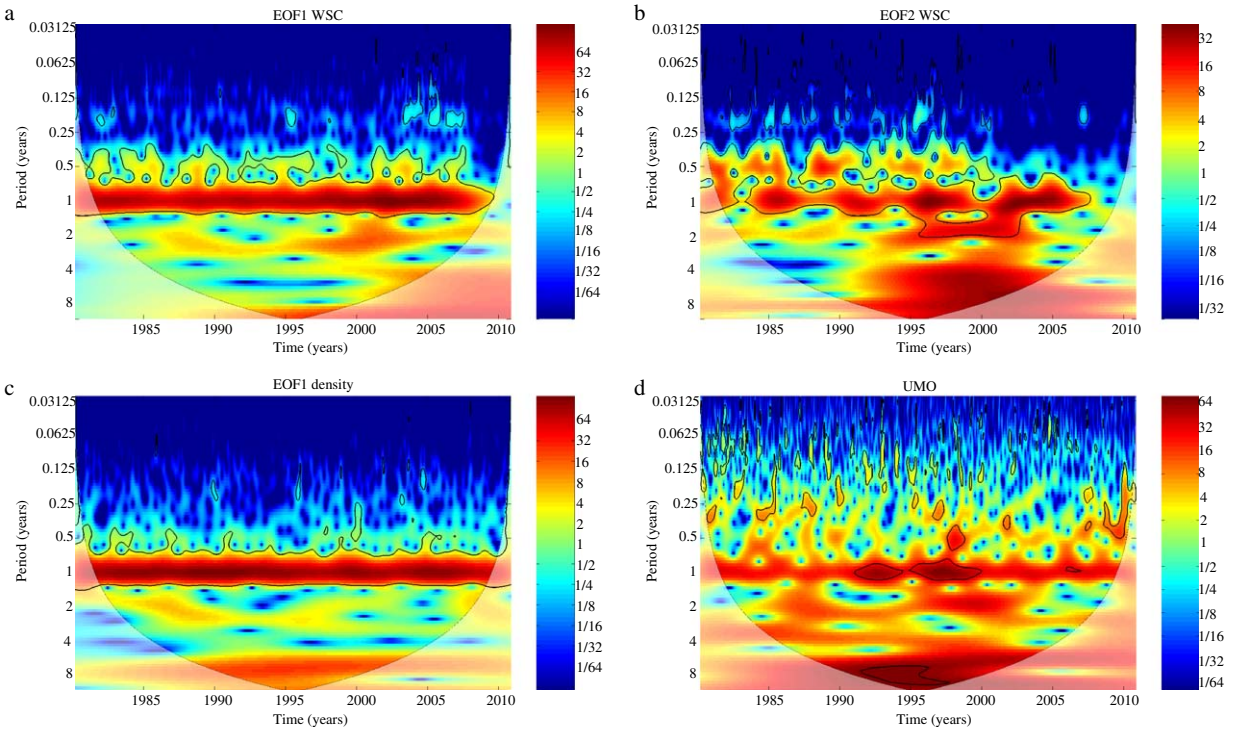

Figure 9. Wavelet analysis for the (a) first and (b) second EOF of wind stress curl, and (c) first EOF of density. Figure 9d shows the wavelet analysis for the UMO transport. Model output from 1980 to 2010 is used to perform this analysis. Black contours represent 95% significance.

do not reveal a continuous significant coherence between the WSC and the density fluctuations at a fixed interannual time scale (Figure 10). For shorter periods of time however, as during 1985–1995, significant coherence is found with a period of 2–3 years between the first modes of WSC and density, with the density leading the WSC fluctuations by 6 months (upward arrows on Figure 10a).

Likewise, the second mode of variability of WSC (Figure 10b) does not lead to density fluctuations at interannual time scales consistently for the whole period 1980–2010. For shorter periods of time, however, significant coherence is found between the WSC north of the islands (EOF 2) and the first mode of variability of density, with the WSC leading the density fluctuations (for example between 1985–1990 and 1998–2005, downward arrows on Figure 10b).

At interannual time scales, although no consistent significant coherence is found between the WSC and the density section at 27.8°N, intermittent significant relationships were found between the patterns of variability of WSC south and north of the islands and the first mode of variability of density. During these periods of time, WSC fluctuations do not necessarily lead density fluctuations, which means that the density fluctuations south of the islands are not primarily driven by the direct pumping from the WSC. Instead, other processes, not yet determined, are responsible for interannual variability in density.

4.5. Link With the Atlantic Meridional Overturning Circulation

One of the primary motivations for this work is to shed light on the processes responsible for the relationship between the winds and the AMOC. In previous observationally based studies of the seasonal cycle of the AMOC at 26°N, a single point location was used for WSC variability, to relate to the single (different) location of the moorings at 1000 m [*Chidichimo et al.*, 2010; *Kanzow et al.*, 2010]. From our EOF analysis of WSC variability, we find that if a different point location had been used for the WSC time series, the relationship between WSC and density at the mooring location would have changed. In section 4.4, we relate the spatial patterns of WSC to density anomalies, and we will now make the connection between the density and the AMOC.

From equation (2), the largest southward transport of UMO is expected when the west to east thermocline tilt—deep to shallow—is strongest. The robust seasonal cycle in the UMO transport can be attributed to the seasonal cycle of WSC, where enhanced cyclonic (anticyclonic) curl in the winter (summer) uplifts

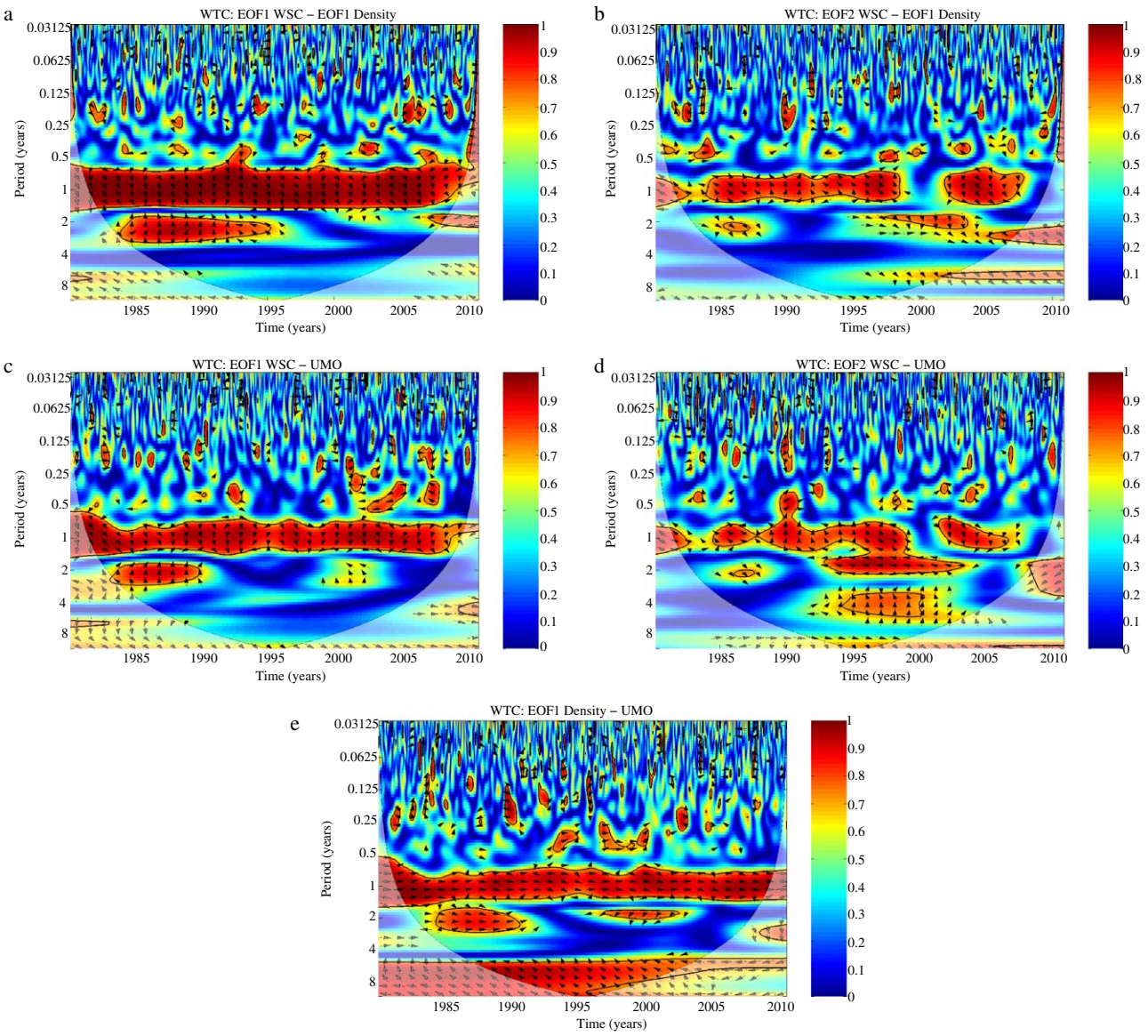

Figure 10. Wavelet transform coherence (WTC) analysis for the period 1980–2010, between (a) the first EOF of wind stress curl (WSC) and the first EOF of density, (b) the second EOF of WSC and the first EOF of density, (c) the first EOF of WSC and the UMO transport, (d) the second EOF of WSC and the UMO transport, and (e) the UMO transport and the first EOF of density using the package of *Grinsted et al*. [2004]. The shading shows the highest correlations between the time series (black contours: 95% confidence level). Arrows indicate the lag at which they occur. If an arrow is pointing to the right, the two time series are in phase, if it is pointing to the left, they are considered as in anti-phase. The deflection of the arrows indicates the lag.

(depresses) isopycnal surfaces, resulting in a peak displacement roughly 3 months later in spring (fall). When isopycnals are at their shallowest at the eastern boundary (i.e., water at 1000 m is denser than usual), the UMO transport reaches its maximum southward values.

The spatial pattern associated with the first EOF of density (Figure 6a) shows negative density anomalies between 700 m and 2000 m. The seasonal cycle of the first EOF of density (Figure 8a) shows a positive peak around October and a negative peak around March–April. These two plots show that in October, the water from 700 m to 2000 m is lighter than usual, while the water between 200 and 700 m is denser than usual. In contrast, in March–April, the amplitude of the seasonal cycle is negative, so the water between 700 m and 2000 m is denser than usual. Figure 8a shows that the UMO transport peaks at the same time, illustrating the link between the density at the eastern boundary and the UMO transport.

Although the UMO transport is more energetic at periods between 5 and 10 years than at seasonal time scales (Figure 9d), the first EOF of density is significantly correlated with the seasonal cycle of the UMO transport with a correlation between these time series of 0.95 (for the period 1980–2010, Figure 8a) and 0.94 (for the period 1980–2001, not shown) at zero lag. The homogeneous correlation map associated with the first EOF of density (Figure 6c) shows that the most significant area of this section is between 1000 m and the bottom. This suggests that these deep density anomalies are responsible for UMO transport anomalies at seasonal time scales. Furthermore, the UMO transport and first mode of variability of density are also coherent and in phase at interannual time scales during 1985–1990 at a period of 2–3 years (Figure 10e). A significant coherence is also found between the UMO transport and first mode of variability of density at longer time scales of 5–10 years. At these time scales, the UMO transport fluctuations precede the density anomalies by about 2.5 years. A possible hypothesis that explains this lag between the UMO transport and the density fluctuations will be further discussed in the conclusion/discussion part of this paper.

The strongest significant coherence between the WSC south of the islands (EOF 1) and the UMO transport is found at seasonal time scales with the WSC leading the UMO by 3 months (Figure 10c). Figure 10d suggests that no continuous link exists between the UMO transport and second mode of WSC at either seasonal or interannual time scales. This suggests that at interannual time scales (2–3 years and longer than 5 years), density fluctuations (first mode) still drive the variability of the UMO transport, but are not driven by the WSC patterns in EOF 1 or 2.

5. Conclusions and Discussion

Using four years of RAPID observations, *Chidichimo et al*. [2010] found a seasonal cycle in in situ density throughout the upper ocean and as deep as 1400 m. *Kanzow et al*. [2010] show that both the eastern and western boundaries contribute to the AMOC variability, but that the eastern boundary drives the robust seasonal variability in the AMOC. However, with only 4 years of data and a relationship between WSC at a single point location with the densities at individual mooring locations raises questions of how representative the results are.

Here we use high-resolution numerical simulations to investigate the relationship between the density structure south of the Canary Islands, the wind stress curl (WSC) around these islands, and the AMOC. We find that the density fluctuations at the eastern boundary of 26°N not only drive the UMO transport at seasonal but also interannual time scales. The 1/12° resolution simulation of the model NEMO (ORCA12) is in good agreement with the RAPID observations and appears to adequately represent the smaller scale features of variability around the Canary Islands including an upwelling filament and eddies (Figure 4). In ORCA12 as in the RAPID observations, the climatological vertical structure in in situ density at the eastern boundary mooring locations (moorings called EBH3 and EBH4/5) is coherent down to roughly 1400 m (Figure 3).

We use empirical orthogonal function (EOF) analysis to understand the spatial patterns of variability in density at 27.84°N south of the Canary Islands (latitude of the RAPID moorings EBH4/5) and in WSC around the islands. The first mode of variability of density explains most of the variability in our area of interest and exhibits three centers of action: the first one from the surface to the bottom of the Ekman layer, the second one from 200 m to 700 m, and the last one from 700 m to the bottom. As the first mode is the only significant mode in our area of interest, it is the only one further analyzed in this paper.

While the first mode of variability of the WSC explains the variability south of the Canary Islands, the second mode shows the variability mainly at the north of the islands. These two modes are significant and show a pattern punctuated by the Canary Islands, indicating the importance of the islands on the WSC pattern.

Although the seasonal cycle dominates the variability of the first modes of density and WSC, the second modes show more interannual variability. At seasonal time scales, the WSC fluctuations south of the islands (first mode) are significantly correlated and precede the first mode of density fluctuations by 3 months. The corresponding principal component is also correlated with the UMO transport with the same lag, and deep density fluctuations (from 700 m to 2000 m) are thus directly linked with the AMOC fluctuations at seasonal time scales. At interannual time scales, during 1985–1990 and for periods of 2–3 years, the first mode of variability of density is significantly coherent and in phase with the UMO transport. For periods between 5 and 10 years, the first mode of variability of density is also significantly coherent with the UMO transport with a

lag around 2.5 years between these two time series, the UMO transport preceding the density anomalies. This lag could be explained by the fact that the UMO transport is driven by density anomalies at the margins [*Hirschi and Marotzke*, 2007]; the RAPID moorings are also placed to ensure a good coverage of the margin densities. However, the EOF of density are calculated using a larger region than the margin itself and the center of action of the first mode of density is located offshore around 15°W (Figure 6a). Consequently, if the density signal first appears along the margin before becoming visible further away from the coast, it could explain a lag between the first EOF of density and the UMO transport at interannual time scales (with the UMO transport preceding an anomaly in the density field).

The second mode of variability of WSC is not continuously significantly coherent with the density field nor the UMO transport thorough the period 1980–2010. This is possibly due to a change in the wind product used to force the simulation in 2001. A clear relationship between the WSC, the density, and the UMO transport has thus been established at seasonal time scales. No continuous link in time (over the 31 year time period) was found between these three fields at interannual time scales, which may be due to an inconsistent wind product used to force the ORCA12 simulation or could result from different processes driving the circulation over different periods.

In the calculation of the AMOC using RAPID observations, the density profile is taken from mooring instruments at a single location. From our results, we can speculate whether the observed seasonal cycle of the AMOC depends on the particular position of the moorings. To investigate this question, Figure 11 shows the (a) amplitude, (b) phase, and (c) fraction of variability explained by the seasonal cycle, for density at 1000 m in the domain chosen. These are determined with a harmonic fit to the time series of density anomaly at each pixel. The eastern extent of the map shows the limit of the 1000 m isobath. The amplitude indicates that the seasonal cycle is most intense at the continental slope. Furthermore, all along the 1000 m isobath, the phase of the seasonal cycle is constant. This suggests that while the seasonal cycle is driven by the seasonal cycle in WSC, which has a variable spatial structure, that at 1000 m throughout the domain considered, the seasonality of the density anomaly is coherent. Thus, the seasonality in density at 1000 m is not strongly dependent on the position of the moorings, as long as the instrument at 1000 m depth is at the 1000 m isobath. In other words, if a tall, deep mooring were further offshore, the data at 1000 m would not have the same seasonal cycle as if it were at the 1000 m isobath.

The previous analyses by *Chidichimo et al*. [2010] and *Kanzow et al*. [2010] used individual locations for WSC to relate to the density anomalies. Here, however, we have shown that the pattern of WSC is spatially variable (Figures 7a and 7b), and that comparisons based on individual locations for the WSC time series may not be robust. Moreover, the spatial pattern of WSC appears highly dependent on the presence of the

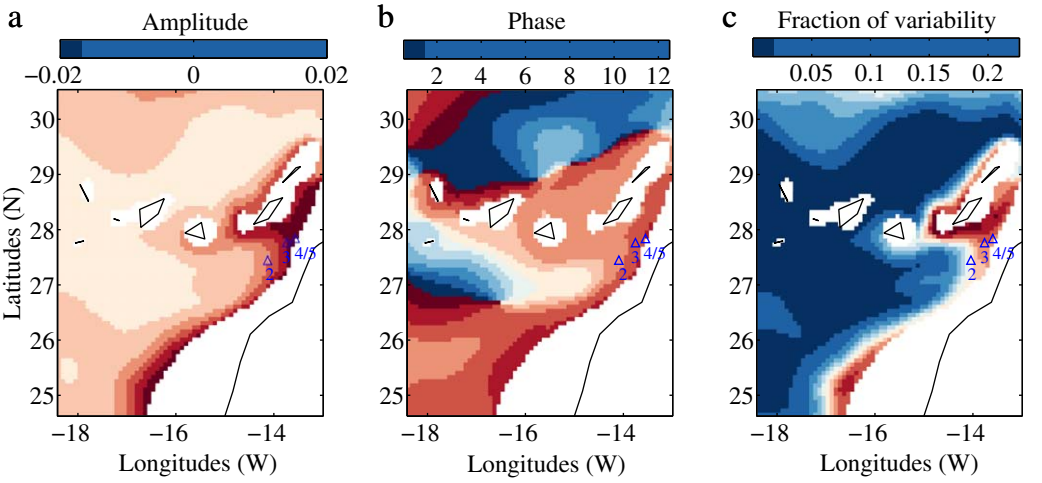

Figure 11. (a) Amplitude, (b) phase, and (c) fraction of variability of the seasonal cycle of density at 1000 m along the eastern boundary, determined with a harmonic fit and using the 31 years of model output. The colorscale of Figure 11b is expressed in months and shows when the seasonal cycle peaks. The locations of the RAPID moorings EBH2, EBH3, and EBH4/5 are represented with blue triangles on each panel of this figure.

Canary Islands, which raises the question of whether the seasonal cycle of the AMOC at 26°N would be different without the islands?

The final point of this discussion is on the impact of the model resolution on the modeled seasonal cycle of the AMOC. Figure 2 compares the seasonal cycle of the AMOC and the UMO transport in different model simulations with different resolutions. While the Canary Islands are not correctly represented in ORCA025 (1/4°) and are absent in ORCA1 (1°, not shown here) (Figure 1), the seasonal cycle in the UMO and AMOC transports are well represented in these lower resolution simulations. The horizontal resolution in the ERA Interim forcing for the ORCA025 simulation is 2.5° and the resolutions of the atmospheric forcings DFS4.1 and DFS5, for ORCA12, are 1.125°. The islands affect the wind stress on spatial scales that are larger than the islands themselves. Even at the resolutions of DFS4.1 and DFS5, the wind stress used to force ORCA1, ORCA025, and ORCA12 always contains the signature of the islands. As a consequence, the ocean model will always "feel" the presence of the islands through the wind stress—whether the model resolution resolves the islands or not. The seasonal cycle of the AMOC in three resolutions of the NEMO model suggests that the WSC still creates upwelling structures, even in the absence of a higher resolution representation of the Canary Islands.

Acknowledgments

Data from the RAPID-WATCH/MOCHA project are funded by the Natural Environment Research Council (NERC) and National Science Foundation (NSF) and are freely available from http://www.rapid.ac.uk/rapidmoc. A. Duchez is supported by NERC and the RAPID project. The model simulation used for this paper was run in the framework of the DRAKKAR project. The authors would like to thank G. D. McCarthy, H. Bryden, and D. Smeed for helpful discussions, as well as the three anonymous reviewers and the editor for their thoughtful comments that significantly helped to improve the manuscript.

References

Arístegui, J., P. Sangrá, S. Hernández-Leon, M. Cantón, A. Hernández-Guerra, and J. L. Kerling (1994), Island-induced eddies in the Canary Islands, *Deep Sea Res., Part I*, *41*, 1509–1525.

Atlas, R., R. N. Hoffman, J. Ardizzone, S. M. Leidner, J. C. Jusem, D. K. Smith, and D. Gambos (2011), A cross-calibrated, multi-platform ocean surface wind velocity product for meteorological and oceanographic applications, *Bull. Am. Meteorol. Soc.*, *92*, 157–174.

Bakun, A., and C. S. Nelson (1991), The seasonal cycle of wind-stress curl in subtropical eastern boundary current regions, *J. Phys. Oceanogr.*, *21*, 1815–1834.

Barnier, B., et al. (2006), Impact of partial steps and momentum advection schemes in a global ocean circulation model at eddy-permitting resolution, *Ocean Dyn.*, *56*, 543–567.

Barton, E. D., et al. (1998), The transition zone of the Canary Current upwelling region, *Prog. Oceanogr.*, *41*, 455–504.

Barton, E. D., J. Arstegui, P. Tett, and E. N. Pérez (2004), Variability in the Canary Islands area of filament-eddy exchanges, *Prog. Oceanogr.*, *62*, 71–94.

Bigg, G. R., T. D. Jickells, P. S. Liss, and T. J. Osborn (2003), The role of the oceans in climate, *Int. J. Climatol.*, *23*, 1127–1159.

Blaker, A. T., J. J.-M. Hirschi, S. Bablu, B. de Cuevas, S. Alderson, A. Coward, and G. Madec (2012), Large near-inertial oscillations of the Atlantic meridional overturning circulation, *Ocean Modell.*, *42*, 50–56.

Brodeau, L., B. Barnier, T. Penduff, A.-M. Treguier, and S. Gulev (2010), An ERA 40 based atmospheric forcing for global ocean circulation models, *Ocean Modell.*, *31*, 88–104.

Chavanne, C., P. Flament, R. Lumpkin, B. Dousset, and A. Bentamy (2002), Scatterometer observations of wind variations induced by oceanic islands: Implications for wind-driven ocean circulation, *Can. J. Remote Sens.*, *28*, 466–474.

Chidichimo, M. P., T. Kanzow, S. A. Cunningham, and J. Marotzke (2010), The contribution of eastern-boundary density variations to the Atlantic meridional overturning circulation at 26.5°N, *Ocean Sci.*, *6*, 475–490.

Dee, D. P., et al. (2011), The ERA-Interim reanalysis: Configuration and performance of the data assimilation system, *Q. J. R. Meteorol. Soc.*, *137*, 553–597.

Delworth, T. L., and R. J. Greatbatch (2000), Multidecadal thermohaline circulation variability driven by atmospheric surface flux forcing, *J. Clim.*, *13*, 1481–1495.

DRAKKAR-Group (2007), Eddy-permitting ocean circulation hindcasts of past decades, *CLIVAR Exch.*, *12*, 8–10.

Eden, C., and J. Willebrand (2001), Mechanism of interannual to decadal variability of the North Atlantic circulation, *J. Clim.*, *14*, 2266–2280.

Fraile-Nuez, E., F. Machín, P. Vélez-Belchí, F. López-Laatzen, R. Borges, V. Benítez-Barrios, and A. Hernández-Guerra (2010), Nine years of mass transport data in the eastern boundary of the North Atlantic subtropical gyre, *J. Geophys. Res.*, *115*, C09009, doi:10.1029/2010JC006161.

Ganachaud, A., and C. Wunsch (2000), Improved estimates of global ocean circulation, heat transport and mixing from hydrographic data, *Nature*, *408*, 453–457.

Ganopolski, A., and S. Rahmstorf (2001), Rapid changes of glacial climate simulated in a coupled climate model, *Nature*, *409*, 153–158.

Getzlaff, J., C. W. Bning, C. Eden, and A. Biastoch (2005), Signal propagation related to the North Atlantic overturning, *Geophys. Res. Lett.*, *32*, L09602, doi:10.1029/2004GL021002.

Grinsted, A., J. C. Moore, and S. Jevrejeva (2004), Application of the cross wavelet transform and wavelet coherence to geophysical time series, *Nonlinear Processes Geophys.*, *11*, 561–566. doi:10.5194/npg-11-561-2004.

Hall, M. M., and H. L. Bryden (1982), Direct estimates and mechanisms of ocean heat transport, *Deep Sea Res., Part A*, *29*, 339–359.

Hernández-Guerra, A., J. Aristegui, and M. Cantón (1993), Phytoplankton pigment patterns in the Canary Islands area as determined using Coastal Zone Colour Scanner data, *Int. J. Remote Sens.*, *14*(7), 1431–1437.

Hirschi, J. J.-M., and J. Marotzke (2007), Reconstructing the meridional overturning circulation from boundary densities and the zonal wind stress, *J. Phys. Oceanogr.*, *37*, 743–763.

Hirschi, J. J.-M., J. Baehr, J. Marotzke, J. Stark, S. A. Cunningham, and J.-O. Beismann (2003), A monitoring design for the Atlantic meridional overturning circulation, *Geophys. Res. Lett.*, *30*(7), 1413, doi:10.1029/2002GL016776.

Hirschi, J. J.-M., A. T. Blaker, B. Sinha, A. Coward, B. de Cuevas, S. Alderson, and G. Madec (2013), Chaotic variability of the meridional overturning circulation on subannual to interannual timescales, *Ocean Sci. Discuss.*, *9*(5), 3191–3238. doi:10.5194/osd-9-3191-2012.

Jiménez, B., P. Sangrà, and E. Mason (2008), A numerical study of the relative importance of wind and topographic forcing on oceanic eddy shedding by tall, deep water islands, *Ocean Modell.*, *22*, 146–157.

Johns, W. E., et al. (2011), Continuous, array-based estimates of Atlantic Ocean heat transport at 26.5°N, *J. Clim.*, *24*(10), 2429–2449.

Kanzow, T., et al. (2007), Flow compensation associated with the meridional overturning, *Science*, *317*, 938–941.

Kanzow, T., et al. (2010), Seasonal variability of the Atlantic Meridional Overturning Circulation at 26.5°N, *J. Clim.*, *23*, 5678–5698.
Knoll, M., A. Hernández-Guerra, B. Lenz, F. L. Laatzen, F. Machín, T. J. Muller, and G. Siedler (2002), The eastern boundary current system between the Canary Islands and the African Coast, *Deep Sea Res., Part II*, *49*, 3427–3440.
Köhl, A. (2005), Anomalies of the meridional overturning: mechanisms in the North Atlantic, *J. Phys. Oceanogr.*, *35*, 1455–1472.
Large, W., and S. Yeager (2004), Diurnal to decadal global forcing for ocean and sea-ice models: The data sets and flux climatologies, *Tech. Note NCAR/TN-460+STR*, 105 pp., CGD Div. of the Natl. Cent. for Atmos. Res., Boulder, Colo.
Machín, F., A. Hernández-Guerra, and J. L. Pelegrí (2006), Mass fluxes in the Canary Basin, *Prog. Oceanogr.*, *70*, 416–447.
Madec, G., and M. Imbard (1996), A global ocean mesh to overcome the North Pole singularity, *Clim. Dyn.*, *12*, 381–388.
Marcello, J., A. Hernández-Guerra, F. Eugenio, and A. Fonte (2011), Seasonal and temporal study of the northwest African upwelling system, *Int. J. Remote Sens.*, *32*(7), 1843–1859.
Matei, D., J. Baehr, J. H. Jungclaus, H. Haak, W. A. Mller, and J. Marotzke (2012), Multiyear prediction of monthly mean Atlantic Meridional Overturning Circulation at 26.5°N, *Science*, *335*, 76–79.
McCarthy, G., E. Frajka-Williams, W. Johns, M. Baringer, C. S. Meinen, H. L. Bryden, D. Rayner, A. Duchez, and S. A. Cunningham (2012), Observed interannual variability of the Atlantic meridional overturning circulation at 26.5°N, *Geophys. Res. Lett.*, *39*, L19609, doi: 10.1029/2012GL052933.
Mielke, C., E. Frajka-Williams, and J. Baehr (2013), Observed and simulated variability of the AMOC at 26°N and 41°N, *Geophys. Res. Lett.*, *40*, 1159–1164, doi:10.1002/grl.50233.
Mittelstaedt, E., D. Pillsbury, and R. L. Smith (1991), The ocean boundary along the northwest African coast: Circulation and oceanographic properties at the sea surface, *Prog. Oceanogr.*, *26*, 307–355.
Nykjaer, L., and L. V. Camp (1994), Seasonal and interannual variability of the coastal upwelling along northwest Africa and Portugal from 1981 to 1991, *J. Geophys. Res.*, *99*, 197–207.
Preisendorfer, R. W. (1988), *Principal Component Analysis in Meteorology and Oceanography*, Elsevier, Amsterdam, 425 pp.
Rayner, D., et al. (2011), Monitoring the Atlantic meridional overturning circulation, *Deep Sea Res., Part II*, *58*, 1744–1753.
Roberts, C. D., et al. (2013), Atmosphere drives recent interannual variability of the Atlantic meridional overturning circulation at 26.5°N, *Geophys. Res. Lett.*, *40*, 5164–5170. doi:10.1002/grl.50930.
Sangrà, P., et al. (2009), The Canary Eddy Corridor: A major pathway for long-lived eddies in the subtropical North Atlantic, *Deep Sea Res., Part I*, *56*(12), 2100–2114.
Sinha, B., B. Topliss, A. T. Blaker, and J.-M. Hirschi (2013), A numerical model study of the effects of interannual time scale wave propagation on the predictability of the Atlantic meridional overturning circulation, *J. Geophys. Res. Oceans*, *118*, 131–146, doi:10.1029/2012JC008334.
Stouffer, R., et al. (2005), Investigating the causes of the response of the thermohaline circulation to past and future climate changes, *J. Clim.*, *19*, 1365–1387.
Trenberth, K. E., and A. Solomon (1994), The global heat balance: Heat transports in the atmosphere and ocean, *Clim. Dyn.*, *10*, 107–134.
Vellinga, M., and R. A. Wood (2002), Global climatic impacts of a collapse of the Atlantic thermohaline circulation, *Clim. Change*, *54*, 251–267.
Zickefeld, K., A. Levermann, M. J. Morgan, T. Kuhlbrodt, S. Rahmstorf, and D. W. Keith (2007), Expert judgements on the response of the Atlantic meridional overturning circulation to climate change, *Clim. Change*, *82*, 235–265.